

# Sequential structural and antiferromagnetic transitions in BaFe<sub>2</sub>Se<sub>3</sub> under pressure

Yang Zhang,<sup>1</sup> Ling-Fang Lin,<sup>1</sup> Jun-Jie Zhang,<sup>1</sup> Elbio Dagotto,<sup>2,3</sup> and Shuai Dong<sup>1,\*</sup>

<sup>1</sup>*School of Physics, Southeast University, Nanjing 211189, China*

<sup>2</sup>*Department of Physics and Astronomy, University of Tennessee, Knoxville, TN 37996, USA*

<sup>3</sup>*Materials Science and Technology Division, Oak Ridge National Laboratory, Oak Ridge, TN 37831, USA*

(Dated: January 4, 2018)

The discovery of superconductivity in the two-leg ladder compound BaFe<sub>2</sub>S<sub>3</sub> has established the 123-type iron chalcogenides as a novel and interesting subgroup of the iron-based superconductors family. However, in this 123 series, BaFe<sub>2</sub>Se<sub>3</sub> is an exceptional member, with a magnetic order and crystalline structure different from all others. Recently, an exciting experiment reported the emergence of superconductivity in BaFe<sub>2</sub>Se<sub>3</sub> at high pressure [J.-J. Ying, H. C. Lei, C. Petrovic, Y.-M. Xiao, and V.-V. Struzhkin, Phys. Rev. B **95**, 241109 (R) (2017)]. In this publication, we report a first principles study of BaFe<sub>2</sub>Se<sub>3</sub>. Our analysis unveils a variety of qualitative differences between BaFe<sub>2</sub>S<sub>3</sub> and BaFe<sub>2</sub>Se<sub>3</sub>, including in the latter an unexpected chain of transitions with increasing pressure. First, by gradually reducing the tilting angle of iron ladders, the crystalline structure smoothly transforms from *Pnma* to *Cmcm* at  $\sim 6$  GPa. Second, the system becomes metallic at 10.4 GPa. Third, its unique ambient pressure Block antiferromagnetic ground state is replaced by the more common CX antiferromagnetic order at  $\sim 12$  GPa, the same magnetic state of the 123-S ladder. This transition is found at a pressure very similar to the experimental superconducting transition. Finally, all magnetic moments vanish at 30 GPa. This reported theoretical diagram of the complete phase evolution is important because of the technical challenges to capture many physical properties in high-pressure experiments. The information obtained in our calculations suggest different characteristics for superconductivity in BaFe<sub>2</sub>Se<sub>3</sub> and BaFe<sub>2</sub>S<sub>3</sub>: in 123-S pairing occurs when magnetic moments vanish, while in 123-Se the transition region from Block- to CX-type magnetism appears to catalyze superconductivity. Finally, an additional superconducting dome above  $\sim 30$  GPa is expected to occur.

## INTRODUCTION

Since the initial discovery of superconductivity in the iron pnictides, the study of iron chalcogenides have rapidly developed into another extensively addressed branch of iron-based superconductors [1–4]. For the vast majority of these novel superconductors, the iron lattice of relevance is quite similar: a slightly distorted two-dimensional iron square lattice stacking along the *c*-axis, where each iron atom is caged in a tetrahedral structure coordinated by pnictogens or chalcogens [3–7]. Different from the iron pnictides, the iron chalcogenides usually display a larger local magnetic moment [3, 8–11] and Fermi surface without hole pockets, implying that the physical mechanism for superconductivity cannot be simply based on Fermi surface nesting considerations in the weak coupling Hubbard *U* limit [1, 3].

Recently, the two-ladder iron chalcogenides, with the 123-type AFe<sub>2</sub>X<sub>3</sub> (*A*=K, Cs, Rb, or Ba; and *X*=S, Se, or Te) chemical composition, have received considerable attention due to their interesting physical properties and unique quasi-one-dimensional structure [12–26] (see Fig. 1). Remarkably, it has been found experimentally that BaFe<sub>2</sub>S<sub>3</sub> is the first iron-ladder that becomes superconducting, under pressures above 10 GPa and with a  $T_c = 24$  K [27, 28]. At ambient conditions, BaFe<sub>2</sub>S<sub>3</sub> is a Mott insulator with the so-called CX-type antiferromagnetic order [see Fig. 1(c), with antiferromagnetic legs and ferromagnetic rungs] below 120 K [27]. This CX order is

sometimes referred to as  $(\pi, 0)$  order as well. Our recent calculation based on density functional theory (DFT) addressed the evolution of the magnetic/electronic properties of BaFe<sub>2</sub>S<sub>3</sub> under pressure [24]. With increasing pressure, we found that the magnetic moments in BaFe<sub>2</sub>S<sub>3</sub> abruptly reduce to zero at a critical pressure. The Mott gap closes slightly in advance, i.e. at a smaller pressure, leading to a non-magnetic (NM) metallic phase, presumably with short-range CX magnetic order, which may be the prerequisite for superconductivity [24]. Similar transitions were also predicted for other members of the 123 series, such as KFe<sub>2</sub>S<sub>3</sub> [24].

BaFe<sub>2</sub>Se<sub>3</sub> is another important member of the iron two-leg ladder family. This material is an antiferromagnetic (AFM) Mott insulator with a robust Néel temperature ( $T_N$ )  $\sim 256$  K [29]. More importantly, BaFe<sub>2</sub>Se<sub>3</sub> is an exceptional member of the 123 series because its physical properties are qualitatively different from others. First, although the members of the 123 series tend to form an orthorhombic structure, the space group of BaFe<sub>2</sub>Se<sub>3</sub> is fairly unique, namely the *Pnma* [30], while all other iron ladders share the more common *Cmcm* space group [27, 29] [see sketches in Figs. 1(a-b)]. The most clear distinction related with the different space groups is the tilting of the ladders that occurs in the 123-Se case. Second, the magnetic ground states are totally different between the BaFe<sub>2</sub>Se<sub>3</sub> and other 123 ladders. More specifically, BaFe<sub>2</sub>Se<sub>3</sub> hosts an exotic block-type AFM order with a large magnetic moment (2.8

$\mu_B/\text{Fe}$ ), as opposed to a CX AFM state. It should be remarked that the block-type AFM order is rare in iron pnictides/chalcogenides, appearing only in a few materials [8, 31, 32]. By contrast, all other 123 ladders host the more conventional CX-type AFM order, with smaller magnetic moments [22, 30, 33]. These two differences are highly nontrivial. For example, the block-type AFM order can drive improper ferroelectricity in the  $Pnma$  structure, rendering  $\text{BaFe}_2\text{Se}_3$  a potential high temperature multiferroic material [34, 35].

Considering its robust magnetic characteristics (large local moments and high  $T_N$  for the block AFM state) [29] and its large band gap ( $> 0.5$  eV from DFT calculation) [34],  $\text{BaFe}_2\text{Se}_3$  seems to be far from superconductivity, according to the empirical knowledge gathered on iron-based superconductors. However, a striking experimental discovery was recently reported in this compound: superconductivity can also be induced in  $\text{BaFe}_2\text{Se}_3$  under high pressure, in the range 10.2-15 GPa [36]. The highest superconducting  $T_c$  reaches  $\sim 10$  K. Interestingly, the local magnetic moments remain considerable large in  $\text{BaFe}_2\text{Se}_3$  under high pressure, as shown using the integrated absolute difference (IAD) analysis. These local magnetic moments reduce to zero only when the pressure reaches 30 GPa. This overall phenomenology is nontrivial, because it means that the superconducting phase emerges directly from a magnetic phase with a large spin moment ( $> 1.3 \mu_B/\text{Fe}$ ). In contrast, for  $\text{BaFe}_2\text{S}_3$  the system is already in a non-magnetic metallic state when pressure is larger than 10.8 GPa, according to DFT calculations [24]. This result is in close proximity to the experimental critical pressure for superconductivity ( $\sim 11$  GPa) [27]. Therefore, the underlying physical mechanisms regarding the superconducting pairing may have different characteristics between  $\text{BaFe}_2\text{S}_3$  and  $\text{BaFe}_2\text{Se}_3$ , which is intriguing. Possible structural and magnetic transitions were also discussed in Ref. [36]. However, due to the technical challenges intrinsic of high pressure experiments, the available experimental information regarding the evolution of crystalline/electronic/magnetic structures remains limited, which prevents a complete understanding of  $\text{BaFe}_2\text{Se}_3$  under pressure. Theory is needed to guide the physical description of this compound.

In this publication, a systematic study of the physical evolution of  $\text{BaFe}_2\text{Se}_3$  under pressure is reported using first-principles DFT calculations. Contrary to the straightforward CX-AFM insulator to NM metal transition observed in  $\text{BaFe}_2\text{S}_3$  with increasing pressure, here a far more complex evolution involving four transitions has been found for  $\text{BaFe}_2\text{Se}_3$ .

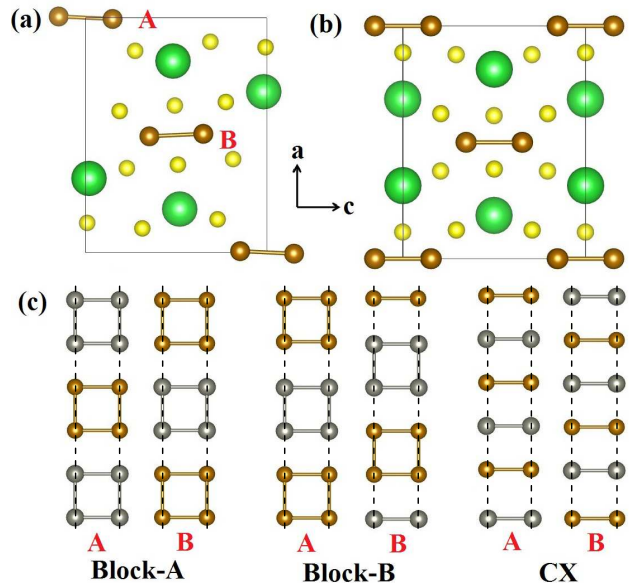


FIG. 1. (a-b) Schematic crystal structures of  $A\text{Fe}_2\text{X}_3$  with the convention: Green = A; Yellow = X; Brown = Fe. (a) corresponds to the space group No. 62  $Pnma$ . (b) corresponds to the space group No. 63  $Cmcm$ . The key difference between these structures is the tilting/non-tilting of the iron ladders. (c) Sketch of some possible spin patterns studied here. Spin up and down are distinguished by colors brown and silver, respectively. A and B are the ladder indexes in one unit cell, as indicated in (a-b). Note A and B are ladders located in different layers.

## METHOD

The DFT calculations were performed using the Vienna *ab initio* simulation package (VASP), with the projector augmented-wave (PAW) potentials [37–39]. The Perdew-Burke-Ernzerhof (PBE) exchange function was employed [40] and the plane-wave cutoff energy was 500 eV. For the block-type AFM order a  $3 \times 3 \times 4$   $k$ -point mesh was used. Since the minimal unit cell is different for different magnetic states, this mesh was appropriately modified for the other various magnetic cells considered (e.g.  $3 \times 7 \times 2$  for the CX-AFM order) to render the  $k$ -point densities approximately the same in reciprocal space. In addition, we have tested that these  $k$ -point meshes already lead to converged energies when compared with denser meshes. Both the lattice constants and atomic positions were fully relaxed until the force on each atom was below  $0.01 \text{ eV}/\text{\AA}$ .

To study the magnetic properties, various possible (in-ladder) magnetic arrangements were imposed on the iron ladders, such as NM, ferromagnetic (FM), CX-AFM, CY-AFM (AFM rungs and FM legs), G-AFM (both rungs and legs AFM), and block-AFM [24]. Despite the dominance of the in-ladder magnetic order, the magnetic cor-

relations between ladders can also slightly affect the energies and physical properties. Therefore, the  $(\pi, \pi, 0)$  order was adopted for the CX-AFM arrangement, as suggested by neutron scattering results and by our previous DFT investigations [24, 34]. Similarly, two types of block-AFM magnetic patterns (Block-A and Block-B) were also considered [34].

In our calculations, starting from the experimental lattice constants under ambient conditions [30], the structures with increasing pressures are obtained via structural optimization in the DFT calculation, since no experimental structural data at different pressures are available thus far.

## RESULTS

### Physical properties under ambient conditions

Before describing the calculations with pressure, the basic DFT results corresponding to  $\text{BaFe}_2\text{Se}_3$  without external pressure are briefly reviewed here. These results were previously reported by some of the authors [34]. In those investigations, it was observed that the pure GGA approach is the best to describe  $\text{BaFe}_2\text{Se}_3$ , consistent with previous DFT calculations of  $\text{BaFe}_2\text{S}_3$  [24, 41]. Thus, the GGA exchange will be adopted for all the following calculations. Our main previous DFT results are summarized in Table I for the benefit of the readers.

First, under ambient conditions, the Block-B magnetic order has the lowest energy among all tested magnetic orders, in agreement with neutron experiments [29]. For the Block-B state, the calculated local magnetic moment of Fe is about  $2.88 \mu_{\text{B}}/\text{Fe}$ , quite close to the experimental value [30]. This moment is much higher than the magnetic moment of  $\text{BaFe}_2\text{S}_3$  ( $\sim 1.2 \mu_{\text{B}}/\text{Fe}$ ) [27].

Second, the calculated lattice constants also agree well with the experimental values [42]. For the Block-B type phase, the Fe-Fe distances are dimerized:  $2.82 \text{ \AA}$  and  $2.58 \text{ \AA}$  due to magnetostriction effects [34], also in agreement with neutron experiments [29].

Third, the energy gap corresponding to the Block-B AFM order is about  $0.5 \text{ eV}$ , in agreement with previous DFT calculations [14, 34]. Although Ref. [15] reported a much smaller gap obtained from transport curves, this discrepancy is probably caused by non-stoichiometry, a quite common phenomenon in  $\text{BaFe}_2\text{Se}_3$ . The optical gap is needed to find the intrinsic band gap.

Fourth, according to the calculated density of states of the Block-B AFM state (not shown here), the bands near the Fermi level are primarily made of Fe- $3d$  orbitals hybridized with Se- $4p$  orbitals, and moreover the Fe atoms are in the high spin state.

TABLE I. The optimized local magnetic moment (in  $\mu_{\text{B}}/\text{Fe}$  unit) within the default PAW sphere, lattice constants ( $\text{\AA}$ ), band gaps (eV) for the various magnetic structures, and energy differences (meV/Fe) with respect to the NM configuration taken as the reference of energy. The experimental values (Exp. for short) are also listed for comparison.

	$M$	$a/b/c$	Gap	Energy
NM	0	11.23/5.38/9.09	0	0
FM	2.96	12.07/5.41/9.2	0	-105.9
CX	2.46	11.94/5.41/9.11	0.11	-261.1
CY	2.82	12.12/5.42/9.24	0.15	-221
Block-A	2.89	12.14/5.40/10.65	0.46	-274.8
Block-B	2.88	12.15/5.40/9.17	0.50	-282.7
Exp.[13]	–	11.93/5.44/9.16	–	–
Exp.[30]	2.8	11.88/5.41/9.14	–	–
Exp.[15]	–	–	0.178	–

### Transitions under pressure

Consider now the effect of hydrostatic pressure when introduced in the calculation. Both the lattice constants as well as the atomic positions are fully relaxed again [24]. The calculated energies for the various magnetic states considered here are shown in Fig. 2(a), as a function of pressure. The Block-B order has the lowest energy until approximately 12 GPa. In that range of pressures, the CX state is slightly higher in energy than Block-A and Block-B, but much lower than others. The crossover between Block-B and CX occurs at  $\sim 12 \text{ GPa}$ , suggesting a pressure induced magnetic phase transition. In fact at  $\sim 12 \text{ GPa}$ , the energy of the Block-B magnetic arrangement displays a sudden jump, and the state becomes degenerate with the NM state. Starting at  $\sim 12 \text{ GPa}$ , the CX state holds the lowest energy until 30 GPa, where all the magnetic states give the same identical energies as the non-magnetic one.

In principle, the enthalpy should be used to determine the phase transition when dealing with the condition of fixed pressure and varying volume, which is common in the context of pressure-induced structural transitions. However, the phase transitions involved here are mainly magnetic-related, instead of structural. The volume difference between the Block-B state and CX state is within 2% in the range of 0-10 GPa. In the experiment (Ref. [36]), the pressure was applied to the sample using diamond anvils at room temperature. Then the sample was cooled down at a fixed volume (fixed by diamond anvils and surrounding wrap). The pressure value at room temperature is used as the experimental value. Strictly speaking, the real experimental conditions were not fixed-pressure, but more likely fixed-volume, which are different from other high pressure experiments on structural transitions. Thus, the most precise theoretical

treatment should be carried out by comparing the total energies of different magnetic orders using the experimental lattice constants, as done in Ref. [43] for pressured  $\text{TbMnO}_3$ . However, since the experimental structural information of  $\text{BaFe}_2\text{Se}_3$  under pressure is unavailable at the current stage, the next-best choice is to use the optimized structure for each magnetic order, as done in our work [44].

With increasing pressure from zero, the local magnetic moment of the iron atoms decreases monotonously, as shown in Fig. 2(b), for all the proposed states. For the interesting Block-B state that is the ground state at ambient conditions, the moment slowly decreases from  $2.88 \mu_{\text{B}}/\text{Fe}$  at 0 GPa to  $2.41 \mu_{\text{B}}/\text{Fe}$  at 11.9 GPa, and then abruptly drops to zero as in a first-order transition, which corresponds also to the sudden jump in energy shown in Fig. 2(a) for this state. By contrast, in the case of the CX phase the local magnetic moment decreases to zero continuously until 30 GPa, resembling a second-order transition. Considering the magnetic ground state transition from Block-B to CX at  $\sim 12$  GPa [Fig. 2(a)], the local magnetic moment should persist to be nonzero in the range from 0 GPa to 30 GPa, which agrees with the experimental observation [36] (in addition, we predict that a sudden reduction in the magnetic moment should be observed experimentally at  $\sim 12$  GPa).

Between approximately 10 and 15 GPa (the region where the superconducting dome was found experimentally), the calculated local magnetic moment is about  $1.75$ - $1.53 \mu_{\text{B}}/\text{Fe}$  for the normal state. This is very close, and only slightly higher, than the experimental value obtained via the IAD analysis at 17 K [36]. It should be noticed that finding overestimated magnetic moments is quite common in DFT calculations of stripe AFM order (C-type) in iron-based superconductors [5, 41, 45, 46], which may due to coexisting localized Fe spins and itinerant electrons. In addition, the methods to estimate the “local” magnetic moments are different between DFT and neutron scattering. In the latter, due to fluctuations, the time averaged magnetic moment is measured and usually this is smaller than the actual instantaneous local moment. This behavior with nonzero moments is conceptually different from that found in  $\text{BaFe}_2\text{S}_3$ , whose local magnetic moment quenches to zero in the normal state corresponding to the superconducting dome region, according to our previous DFT calculations [24].

The band gaps of various magnetic orders are displayed in Fig. 2(c). With increasing pressure, all gaps decrease monotonously and eventually close. Considering the aforementioned magnetic transition, the system persists to be insulating until the collapse of the Block-B state gap, beyond which the system is metallic even still within the Block-B magnetic state. The critical pressure (10.4 GPa) for this insulator-metal transition is also very similar to the experimental observation (10.2 GPa for metallic behavior at low temperatures) [36]. After

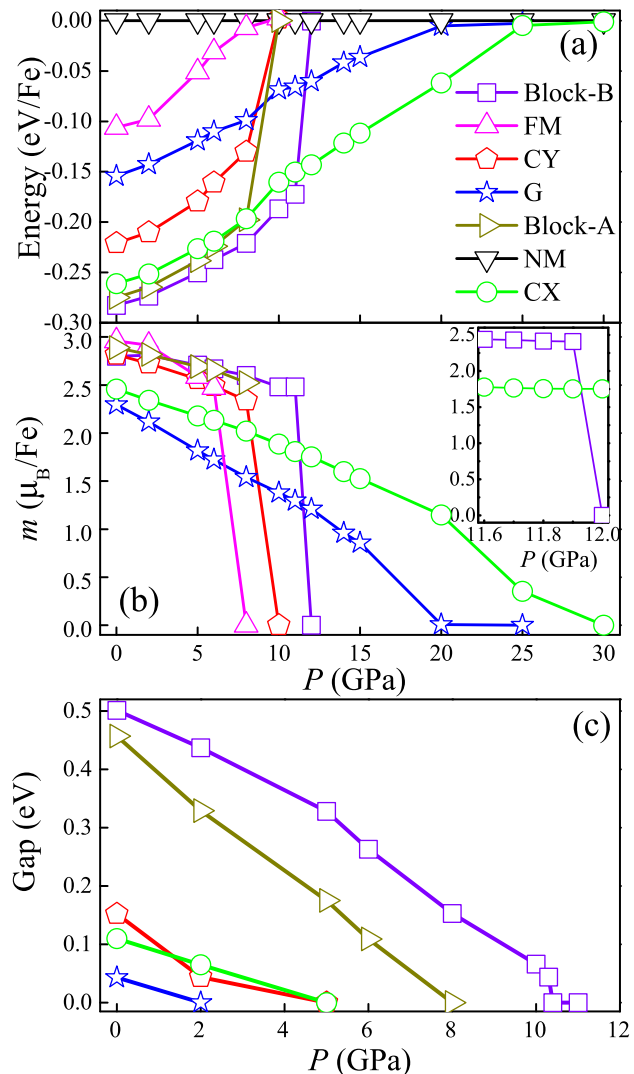


FIG. 2. Evolution of the magnetic and electronic structures of  $\text{BaFe}_2\text{Se}_3$  as a function of pressure. (a) Energies (per Fe) of the various magnetic orders indicated. (b) Local magnetic moments of Fe, integrated within the default Wigner-Seitz sphere as specified by VASP. *Inset*: an amplified view near the transition. (c) Band gaps for the many states analyzed.

the magnetic order of the Block-B phase collapses at  $\sim 12$  GPa, then the ground state is metallic and has CX order.

In addition to the changes in the magnetic state and iron moments, a structural evolution has also been observed, as shown in Fig. 3(a). As schematically displayed in the inset, in Fig. 3(a) we show the tilting angle of the iron ladders, defined as  $\theta$ , with respect to the  $b-c$  plane. Its nonzero value is the main difference between the  $Pnma$  ( $\text{BaFe}_2\text{Se}_3$ ) and  $Cmcm$  structures (other  $\text{AFe}_2\text{X}_3$ 's). Under pressure, this tilting angle gradually decreases to  $0^\circ$  at  $\sim 6$  GPa, implying a structural transition from  $\text{BaFe}_2\text{Se}_3$  ( $Pnma$ ) into  $\gamma\text{-BaFe}_2\text{Se}_3$

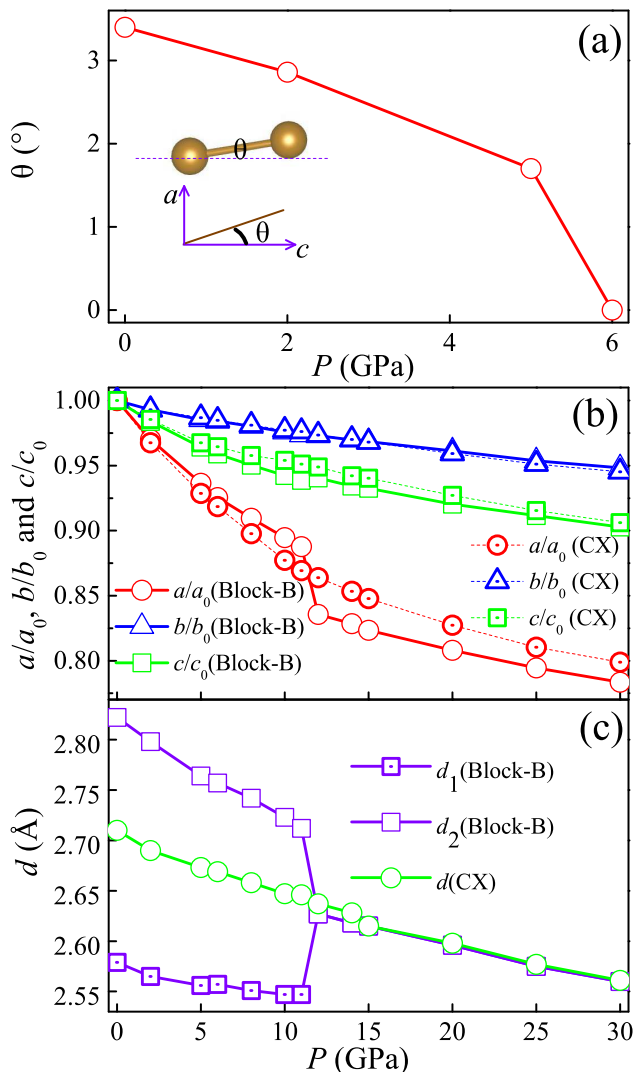


FIG. 3. Evolution of the crystalline structure of BaFe<sub>2</sub>Se<sub>3</sub> varying pressure. (a) The tilting angle of the iron ladders in the Block-B magnetic state (see sketch in panel (a) of Fig. 1). (b) Lattice constants, normalized to the original ones at zero pressure. (c) The Fe-Fe distance along the leg ladder direction. In both (b) and (c), the results for the dominant CX and Block-B phases are shown for comparison. In (c), there are two distances for the Block-B phase because there are two types of bonds along the legs: AFM and FM.

(*Cmcm*) [47].

Figure 3(b) is a measure of the anisotropic compressibility, illustrating that fact that the lattice is softest along the  $a$ -axis (perpendicular to the ladders) and hardest along the  $b$ -axis (the leg direction of the ladders). This is reasonable: the key substructures of the crystal are the two-leg ladders that are difficult to modify with pressure. Such anisotropic compressibility is qualitatively similar for all the 123 series, due to the spare space between ladders and the compact bonds along ladders [24]. The magnetic transition at 12 GPa also leads to a discontinuous

change in the lattice constants, although the space group remains the same. The tetramerization of the Block-B magnetic state, characterized by a disproportionation of the Fe-Fe bond lengths, is suppressed by increasing pressure from zero. At the critical pressure ( $\sim 12$  GPa), the structural tetramerization suddenly disappears, accompanying the magnetic transition, as summarized in Fig. 3(c).

## DISCUSSION

According to the results gathered in this study, it is possible to sketch a theoretical phase diagram for BaFe<sub>2</sub>Se<sub>3</sub> under pressure, as shown in Fig. 4(a). With increasing pressure, the structural transition occurs first at 6 GPa, with second order characteristics. The *Pnma* group in the AFe<sub>2</sub>X<sub>3</sub> structure changes to the more common *Cmcm* group. No electronic/magnetic anomaly is visible at this structural transition. As the pressure continues increasing, an insulator-metal transition occurs at 10.4 GPa, slightly before the magnetic transition (from Block-B to CX states) that takes place at 12 GPa. Remarkably, the experimentally observed superconducting dome (pairing is beyond the capabilities of DFT) emerges very close to the theoretical boundary between the Block-B and CX magnetic states. Finally, the CX phase persists until a very high pressure of approximately 30 GPa where all magnetic moments vanish. This phase diagram, including the evolution of the local magnetic moments, either agrees well or is compatible with the available experimental data. In addition, our results also provide additional systematic information, such as the unexpected transition from Block-B to CX states. This transition is difficult to observe experimentally because of the challenges in dealing with high pressure setups.

For comparison, the phase diagram of BaFe<sub>2</sub>S<sub>3</sub> is shown in Fig. 4(b), based on data from previous DFT [24] and experimental efforts [23, 27]. This phase diagram is much simpler. In this case the system turns directly from an insulator with CX magnetic order to a non-magnetic metal with increasing pressure, and the experimental superconducting dome emerges at the CX-NM boundary. As a reasonable conclusion of the S-based phase diagram, the driving force of superconductivity may be attributed to short-range magnetic fluctuations of CX-type in the non-magnetic state. However, according to DFT the driving force of superconductivity in BaFe<sub>2</sub>Se<sub>3</sub> appears to be induced, instead, by the competition between Block-B and CX magnetic orders. This is an exotic scenario because it involves two states with long-range magnetic order, and a first-order-like transition between them, contrary to the more established framework with magnetic and nonmagnetic states as in BaFe<sub>2</sub>S<sub>3</sub>. This difference may be the reason why the highest superconducting  $T_c$  in the Se-ladder is considerably lower than in the S-ladder.

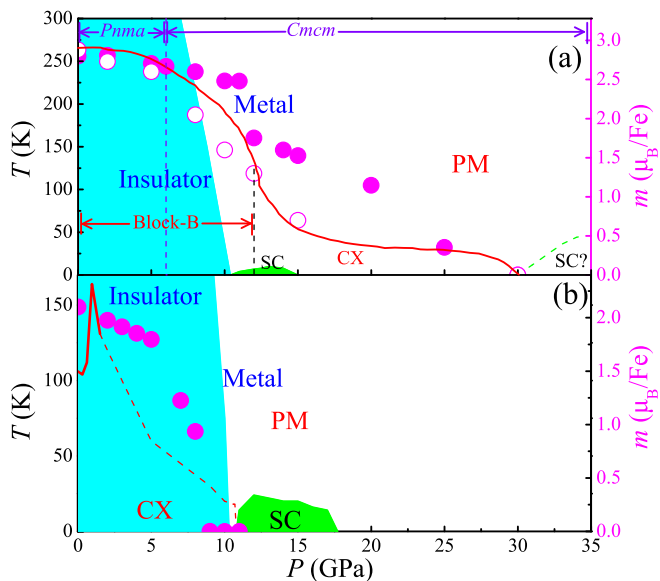


FIG. 4. Phase diagram of  $\text{BaFe}_2\text{X}_3$  ( $X = \text{S}, \text{Se}$ ) varying pressure, according to experimental data [27, 30, 36] and to present and previous [24] DFT calculations. The curves of AFM Néel temperatures (red solid), including the superconducting (SC) domes, are all from experiments. For example, see Fig. 4 of Ref. [36]. (a) Results for  $\text{BaFe}_2\text{Se}_3$ . The superconducting dome beyond 30 GPa is a theoretical prediction, to be verified in future experiments. (b) Results for  $\text{BaFe}_2\text{S}_3$ . The dashed portion of the curve for  $T_N$  is an assumed smooth drop with increasing pressure (experimental data is lacking). Right axis: local magnetic moments. Open symbols: experimental data at low temperature. Solid symbols: DFT data (at zero temperature).

In spite of these differences, it is interesting to note that in both materials the local magnetic moments fast drop by  $\sim 1 \mu_B/\text{Fe}$  just before the appearance of the superconducting dome. In this sense, the spin fluctuations are somewhat similar in  $\text{BaFe}_2\text{S}_3$  and  $\text{BaFe}_2\text{Se}_3$  at the critical points. Of course, the physical mechanism(s) for superconductivity in these two system needs further theoretical and experimental investigations.

In addition, according to the experience gathered on  $\text{BaFe}_2\text{S}_3$ , an interesting speculation for  $\text{BaFe}_2\text{Se}_3$  is that another superconducting dome, potentially with a higher  $T_C$ , may exist a little above 30 GPa.

To better understand the underlying driving force for pressure-driven phase transitions in  $\text{BaFe}_2\text{Se}_3$ , the band structure of the NM state at 0 GPa and 12 GPa are displayed in Figs. 5(a-b). This figure reveals a clear tendency for the bandwidths of the iron  $3d$  bands to be enlarged upon pressure, implying an enhancement of itinerant properties of the  $3d$  electrons.

Moreover, the band structures for magnetic ground states are displayed in Figs. 5(c-d) at 0 GPa and 12 GPa, respectively. These two band structures are rather different, making it impossible to extract more basic driving

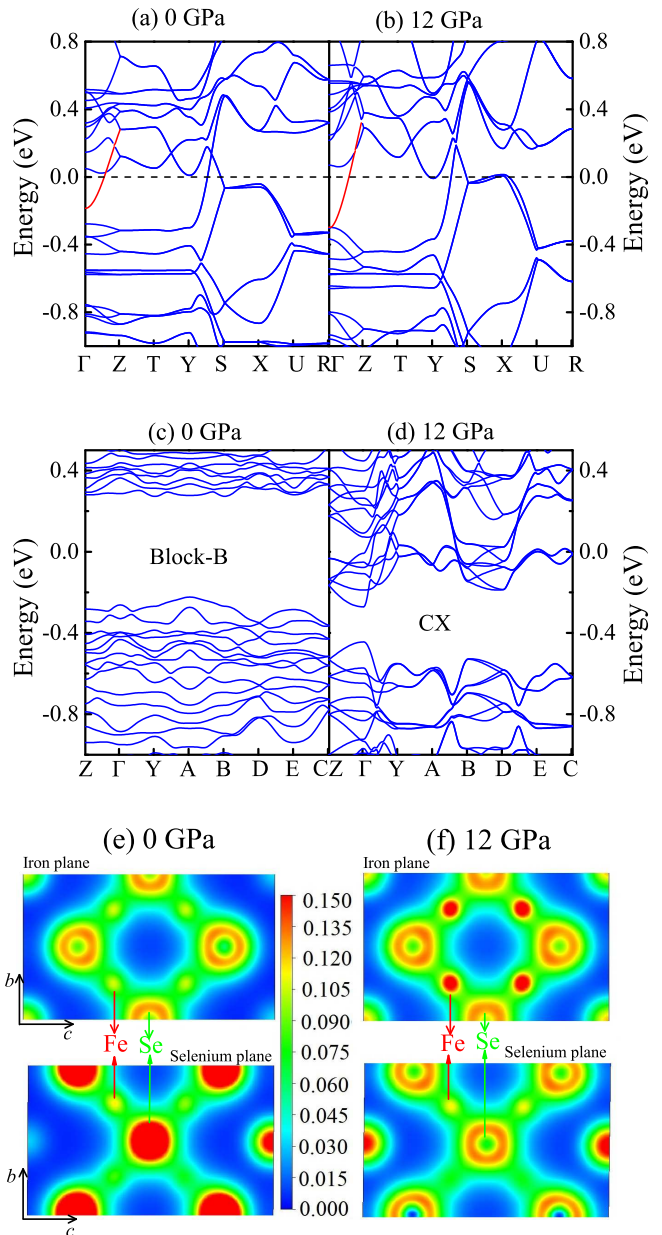


FIG. 5. Electronic structure of  $\text{BaFe}_2\text{Se}_3$ , from DFT. (a-b) Band structures at 0 GPa and 12 GPa for the hypothetical NM state for comparison. The Fermi level is shown with dashed lines. The bandwidths of the iron bands increase with increasing pressure (e.g. see the branch highlighted in red). (c-d) Band structures at 0 GPa (Block-B) and 12 GPa (CX) for the magnetic states for comparison. (e-f) Electron density profiles of the iron ladders at 0 GPa and 12 GPa for the hypothetical NM state for comparison. The increase in the red intensity of the iron atoms at 12 GPa, as compared to 0 GPa, is indicative of electronic doping by pressure. Upper panel: cut in an iron ladder plane; Lower panel: cut in a Se plane.

forces behind the magnetic transition. Thus, the above discussion based on the hypothetical NM state instead of the real magnetic state is valuable to reveal the direct pressure effects to the band structure.

The electronic density profiles of the iron ladders are correspondingly shown in Figs. 5(e-f). It is clear that the electronic density at the iron sites increases with increasing pressure. In fact, according to the Bader charge analysis [48, 49], electrons transfer from Se to Fe atoms by an amount 0.18 electron/Fe when the pressure increases from 0 GPa to 12 GPa. This tendency is equivalent to doping the system with electrons: increasing pressure amounts to adding electrons to the ladders. This same conclusion was reached in previous DFT investigations of  $\text{BaFe}_2\text{S}_3$  under high pressure [24]. This phenomenon is compatible with recent Density Matrix Renormalization Group (DMRG) technique results where pairing of carriers was unveiled by doping the parent state of two-leg ladders, modeled with a two-orbital Hubbard model [25, 26]. This general tendency of pressure inducing doping of ladders was previously observed experimentally in two-leg Cu-oxide ladders as well [50]. In this case hole pairing was theoretically predicted upon doping the system and later confirmed experimentally [51–53].

## CONCLUSIONS

The pressure effects on  $\text{BaFe}_2\text{Se}_3$  have been investigated using first-principles calculations. The existence of several sequential transitions, including structural, electronic, and magnetic transitions, have been revealed by our calculations. First, the crystalline structure transition from  $Pnma$  to  $Cmcm$  occurs at 6 GPa and it is a smooth second order transition, which does not affect strongly any other physical properties. Then, an insulator-metal transition happens at 10.4 GPa, acting as a precursor of the magnetic transition from the (unusual) Block-B antiferromagnetic state to the (more common) CX antiferromagnetic state at  $\sim 12$  GPa. Finally, all magnetic moments quench to zero at  $\sim 30$  GPa.

Our calculations have not only reproduced several experimental observations (e.g. magnetic-nonmagnetic transition at  $\sim 30$  GPa and insulator-metal transition at  $\sim 10$  GPa) but they have also provided a systematic description of the phase evolution of  $\text{BaFe}_2\text{Se}_3$  under high pressure. In addition, according to our phase diagram, we conjecture that the experimentally observed superconducting dome could be induced by magnetic fluctuations due to the competition between the two dominant magnetic states Block-B and CX, which is unexpected since superconducting phases in electronic correlated systems are usually observed at the transition from a magnetic state with long-range order to a non-magnetic state with short-range order. Moreover, by analogy with what occurs in  $\text{BaFe}_2\text{S}_3$  we believe that an additional supercon-

ducting dome, potentially with an even higher  $T_c$ , could exist beyond 30 GPa when the CX state is replaced by a non-magnetic state. Overall, it is clear that ladder compounds in the iron-superconductors context have rich phase diagrams. Moreover, pairing calculations in model Hamiltonians are easier in one dimension than higher, due to the availability of powerful computational techniques. For all these reasons, the iron ladder materials have much potential to solve the mysteries of iron-based high critical temperature superconductors.

We acknowledge valuable discussions with H.-C. Lei, K. Yamauchi, S. Picozzi, N. Patel, and Y.-F. Zhang. We also thank J.-J. Ying, V.-V. Struzhkin, and C. Petrovic for share their preprint before publication. This work was supported by National Natural Science Foundation of China (Grant No. 11674055). L.F.L. was supported by Jiangsu Innovation Projects for Graduate Students (Grant No. KYCX17\_0047). E.D. was supported by the U.S. Department of Energy, Office of Basic Energy Sciences, Materials Sciences and Engineering Division. Most calculations were carried out at the National Supercomputer Center in Guangzhou (Tianhe-II).

---

\* Corresponding author. E-mail: sdong@seu.edu.cn

- [1] P. C. Dai, J. P. Hu, and E. Dagotto, *Nature Phys.* **8**, 709 (2012).
- [2] G. R. Stewart, *Rev. Mod. Phys.* **83**, 1589 (2011).
- [3] E. Dagotto, *Rev. Mod. Phys.* **85**, 849 (2013).
- [4] P. C. Dai, *Rev. Mod. Phys.* **87**, 855 (2015).
- [5] I. I. Mazin and M. D. Johannes, *Nature Phys.* **5**, 141 (2009).
- [6] D. C. Johnston, *Adv. Phys.* **59**, 803 (2010).
- [7] Q. M. Si, R. Yu, and E. Abrahams, *Nature Rev. Mater.* **1**, 16017 (2016).
- [8] W. Li, H. Ding, P. Deng, K. Chang, C. L. Song, K. He, L. L. Wang, X. C. Ma, J. P. Hu, X. Chen, and Q. K. Xue, *Nature Phys.* **8**, 126 (2012).
- [9] M. Wang, W. Tian, P. Valdivia, S. X. Chi, E. Bourret-Courchesne, P. C. Dai, and R. J. Birgeneau, *Phys. Rev. B* **90**, 125148 (2014).
- [10] Y. Zhang, L.-F. Lin, J.-J. Zhang, X. Huang, M. An, and S. Dong, *Phys. Rev. Mater.* **1**, 034406 (2017).
- [11] W. Bao, Q. Z. Huang, G. F. Chen, M. A. Green, D. M. Wang, J. B. He, and Y. M. Qiu, *Chin. Phys. Lett.* **28**, 086104 (2011).
- [12] A. Krzton-Maziopa, E. Pomjakushina, V. Pomjakushin, D. Sheptyakov, D. Chernyshov, V. Svitlyk, and K. Conder, *J. Phys.: Condens. Matter* **23**, 402201 (2011).
- [13] Y. Nambu, K. Ohgushi, S. Suzuki, F. Du, M. Avdeev, Y. Uwatoko, K. Munakata, H. Fukazawa, S. X. Chi, Y. Ueda, and T. J. Sato, *Phys. Rev. B* **85**, 064413 (2012).
- [14] B. Saparov, S. Calder, B. Sipos, H. B. Cao, S. X. Chi, D. J. Singh, A. D. Christianson, M. D. Lumsden, and A. S. Sefat, *Phys. Rev. B* **84**, 245132 (2011).
- [15] H. Lei, H. Ryu, A. I. Frenkel, and C. Petrovic, *Phys. Rev. B* **84**, 214511 (2011).
- [16] F. Du, K. Ohgushi, Y. Nambu, T. Kawakami, M. Avdeev,

- Y. Hirata, Y. Watanabe, T. J. Sato, and Y. Ueda, Phys. Rev. B **85**, 214436 (2012).
- [17] Q. Luo, A. Nicholson, J. Rincón, S. Liang, J. Riera, G. Alvarez, L. Wang, W. Ku, G. D. Samolyuk, A. Moreo, and E. Dagotto, Phys. Rev. B **87**, 024404 (2013).
- [18] C. Monney, A. Uldry, K. J. Zhou, A. Krzton-Maziopa, E. Pomjakushina, V. N. Strocov, B. Delley, and T. Schmitt, Phys. Rev. B **88**, 165103 (2013).
- [19] Y. Hirata, S. Maki, J.-I. Yamaura, T. Yamauchi, and K. Ohgushi, Phys. Rev. B **92**, 205109 (2015).
- [20] M. Mourigal, S. Wu, M.-B. Stone, J.-R. Neilson, J.-M. Caron, T.-M. McQueen, and C.-L. Broholm, Phys. Rev. Lett. **115**, 047401 (2015).
- [21] R. Arita, H. Ikeda, S. Sakai, and M.-T. Suzuki, Phys. Rev. B **92**, 054515 (2015).
- [22] M. Wang, M. Yi, S. J. Jin, H. C. Jiang, Y. Song, H. Q. Luo, A. D. Christianson, C. de la Cruz, E. Bourret-Courchesne, D. X. Yao, D. H. Lee, and R. J. Birgeneau, Phys. Rev. B **94**, 041111(R) (2016).
- [23] S. X. Chi, Y. Uwatoko, H. B. Cao, Y. Hirata, K. Hashizume, T. Aoyama, and K. Ohgushi, Phys. Rev. Lett. **117**, 047003 (2016).
- [24] Y. Zhang, L. F. Lin, J. J. Zhang, E. Dagotto, and S. Dong, Phys. Rev. B **95**, 115154 (2017).
- [25] N. D. Patel, A. Nocera, G. Alvarez, R. Arita, A. Moreo, and E. Dagotto, Phys. Rev. B **94**, 075119 (2016).
- [26] N. D. Patel, A. Nocera, G. Alvarez, A. Moreo, and E. Dagotto, Phys. Rev. B **96**, 024520 (2017).
- [27] H. Takahashi, A. Sugimoto, Y. Nambu, T. Yamauchi, Y. Hirata, T. Kawakami, M. Avdeev, K. Matsubayashi, F. Du, C. Kawashima, H. Soeda, S. Nakano, Y. Uwatoko, Y. Ueda, T. J. Sato, and K. Ohgushi, Nature Mater. **14**, 1008 (2015).
- [28] T. Yamauchi, Y. Hirata, Y. Ueda, and K. Ohgushi, Phys. Rev. Lett. **115**, 246402 (2015).
- [29] J. M. Caron, J. R. Neilson, D. C. Miller, K. Arpino, A. Llobet, and T. M. McQueen, Phys. Rev. B **85**, 180405(R) (2012).
- [30] J. M. Caron, J. R. Neilson, D. C. Miller, A. Llobet, and T. M. McQueen, Phys. Rev. B **84**, 180409(R) (2011).
- [31] Y. Zhang, H. M. Zhang, Y. K. Weng, L. F. Lin, X. Y. Yao, and S. Dong, Phys. Status solidi-Rapid Res. Lett. **10**, 757 (2016).
- [32] F. Ye, S. Chi, W. Bao, X. F. Wang, J. J. Ying, X. H. Chen, H. D. Wang, C. H. Dong, and M. H. Fang, Phys. Rev. Lett. **107**, 137003 (2011).
- [33] M. Wang, S. J. Jin, M. Yi, Y. Song, H. C. Jiang, W. L. Zhang, H. L. Sun, H. Q. Luo, A. D. Christianson, C. de la Cruz, E. Bourret-Courchesne, D. X. Yao, D. H. Lee, and R. J. Birgeneau, Phys. Rev. B **96**, 060502(R) (2017).
- [34] S. Dong, J.-M. Liu, and E. Dagotto, Phys. Rev. Lett. **113**, 187204 (2014).
- [35] S. W. Lovesey, D. D. Khalyavin, and G. van der Laan, Phys. Scr. **91**, 015803 (2016).
- [36] J.-J. Ying, H. C. Lei, C. Petrovic, Y.-M. Xiao, and V.-V. Struzhkin, Phys. Rev. B **95**, 241109(R) (2017).
- [37] G. Kresse and J. Hafner, Phys. Rev. B **47**, 558 (1993).
- [38] P. E. Blöchl, O. Jepsen, and O. K. Andersen, Phys. Rev. B **49**, 16223 (1994).
- [39] J. P. Perdew, K. Burke, and M. Ernzerhof, Phys. Rev. Lett. **77**, 3865 (1996).
- [40] G. Kresse and J. Furthmüller, Phys. Rev. B **54**, 11169 (1996).
- [41] M. T. Suzuki, R. Arita, and H. Ikeda, Phys. Rev. B **92**, 085116 (2015).
- [42] The small discrepancy of lattice constants between theory and experiments along the  $a$ -axis is probably due to the complex magnetic coupling between ladders along that  $a$ -axis, as discussed in Ref. [35]. However, a very large cluster is required to accommodate such a complex magnetic coupling, beyond the goals of the present study.
- [43] T. Aoyama, K. Yamauchi, A. Iyama, S. Picozzi, K. Shimizu, and T. Kimura, Nature Commun. **5**, 4927 (2014).
- [44] We also tested the use of the enthalpy to determine the phase transitions. Unfortunately, using calculations based on enthalpy, a premature phase transition from Block-B to CX order occurs at  $\sim 3$  GPa, together with the insulator-metal transition, which is very different from the available experimental information (insulator-metal transition occurs at 10 GPa). Although a fine tuning of the Hubbard  $U$  in the DFT+ $U$  formalism can be used so that the insulator-metal transition matches the experimental value, the side effect is that there is a robust magnetic state at 30 GPa, which is different from the experimental information. In summary, the use of the enthalpy leads to large discrepancies between the theoretical and experimental phase diagrams even if  $U$  is tuned.
- [45] P. Hansmann, R. Arita, A. Toschi, S. Sakai, G. Sangiovanni, and K. Held, Phys. Rev. Lett. **104**, 197002 (2010).
- [46] Z. P. Yin, K. Haule, and G. Kotliar, Nature Mater. **10**, 932 (2011).
- [47] V. Svitlyk, D. Chernyshov, E. Pomjakushina, A. Krzton-Maziopa, K. Conder, V. Pomjakushin, R. Pöttgen, and V. Dmitriev, J. Phys.: Condens. Matter **25**, 315403 (2013).
- [48] R. F. W. Bader, Atoms in molecules (Wiley Online Library, 1990).
- [49] G. Henkelman, A. Arnaldsson, and H. Jónsson, Comput. Mater. Sci. **36**, 354 (2006).
- [50] Y. Piskunov, D. Jérôme, P. Auban-Senzier, P. Wzietek, and A. Yakubovsky, Phys. Rev. B **72**, 064512 (2005).
- [51] E. Dagotto and T. M. Rice, Science **271**, 618 (1996).
- [52] E. Dagotto, Rep. Prog. Phys. **62**, 1525 (1999).
- [53] M. Uehara, T. Nagata, J. Akimitsu, H. Takahashi, N. Mori, and K. Kinoshita, J. Phys. Soc. Jpn. **65**, 2764 (1996).